Journal of Applied Physics

Ultrathin two-dimensional van der Waals asymmetric ferroelectric semiconductor junctions

Cite as: J. Appl. Phys. **132**, 054101 (2022); https://doi.org/10.1063/5.0098827
Submitted: 12 May 2022 • Accepted: 07 July 2022 • Published Online: 01 August 2022

Dongqi Zheng, Mengwei Si, Sou-Chi Chang, et al.

Journal of Applied Physics ARTICLE scitation.org/journal/jap

Ultrathin two-dimensional van der Waals asymmetric ferroelectric semiconductor junctions

Cite as: J. Appl. Phys. **132**, 054101 (2022); doi: 10.1063/5.0098827
Submitted: 12 May 2022 · Accepted: 7 July 2022 ·
Published Online: 1 August 2022

View Online Export Citation CrossMark

Dongqi Zheng,[1,2] Mengwei Si,[1,2] Sou-Chi Chang,[3] Nazila Haratipour,[3] Zhizhong Chen,[1,2] Adam Charnas,[1,2] Shouyuan Huang,[2,4] Kang Wang,[2,5] Letian Dou,[2,5] Xianfan Xu,[2,4] Uygar E. Avci,[3] and Peide D. Ye[1,2,a)]

AFFILIATIONS

[1]Elmore Family School of Electrical and Computer Engineering, Purdue University, West Lafayette, Indiana 47907, USA
[2]Birck Nanotechnology Center, Purdue University, West Lafayette, Indiana 47907, USA
[3]Components Research, Intel Corporation, Hillsboro, Oregon 97124, USA
[4]School of Mechanical Engineering, Purdue University, West Lafayette, Indiana 47907, USA
[5]Davidson School of Chemical Engineering, Purdue University, West Lafayette, Indiana 47907, USA

Note: This paper is part of the Special Topic on 2D Piezoelectrics, Pyroelectrics, and Ferroelectrics.
a)Author to whom correspondence should be addressed: yep@purdue.edu

ABSTRACT

Two-dimensional van der Waals ferroelectric semiconductors have attracted extensive research interest in both theoretical investigation and device applications due to their ferroelectricity and semiconducting nature. However, it is still not well understood how the ferroelectric phase is able to coexist with the semiconducting phase in this emerging material class. In this work, mm-scale continuous films of In_2Se_3 with a thickness of ~3 nm were synthesized successfully by physical vapor deposition. Furthermore, we fabricated asymmetric ferroelectric semiconductor junctions (a-FSJs) from thick exfoliated and PVD-grown ultrathin In_2Se_3 films. A high read current density of ~100 A/cm^2 and a distinction ratio of over 10^2 at $V_{Read} = 0.5$ V are achieved in devices fabricated by a 3 nm-thick In_2Se_3 film toward ultrahigh-density memory integration. Notably, the coercive voltage is constant, with In_2Se_3 film thickness decreasing from 200 to 3 nm. A qualitative model is proposed to elucidate the anomalous film-thickness-independent coercive voltage in this ultrathin a-FSJ, which can also be generalized to other emerging two-dimensional ferroelectric semiconductors.

I. INTRODUCTION

Van der Waals (vdW) ferroelectric (FE) materials have attracted significant interest because of their atomically uniform thicknesses, clean interfaces, room-temperature ferroelectricity, and semiconducting properties.[1–3] Ferroelectricity in vdW layered materials has been theoretically predicted and experimentally verified, such as $CuInP_2S_6$,[4] IV–VI compounds (SnTe[5] and SnSe[6]), and α-In_2Se_3.[7,8] The coupling of two-dimensional semiconductor nature and layer-by-layer ferroelectric switching has inspired the research of in-plane ferroelectricity[9] and novel memory device applications driven by out-of-plane polarization.[10–12]

Among the two-dimensional (2D) vdW FE materials, α-In_2Se_3 is considered a promising candidate due to its moderate bandgap of 1.4 eV, room temperature ferroelectricity, and the potential feasibility for large area growth. These properties provide an appealing platform for research into new physical phenomena such as 2D multiferroic heterostructures[11] and practical applications such as ultrahigh-density non-volatile memristors.[13–15] Different from the traditional ferroelectric switching mechanism, the ferroelectricity in In_2Se_3 is driven by Se–In covalent bond breaking and reformation when middle layer Se atoms move laterally under an external electric field, rather than by long-range interactions, and such strong covalent bonds can prevent the depolarization field from suppressing the polarization even when the thickness is scaled down to 3 nm.[16] Employing the coupled properties of vdW semiconductors and ferroelectrics, many novel devices were proposed, such as the

ferroelectric semiconductor field-effect transistor (FeS-FET)[17,18] and asymmetric ferroelectric semiconductor junction (a-FSJ),[19] which are regarded as potential solutions to the charge injection from the high field across the under-layer in the traditional Si ferroelectric field-effect transistor (FeFET) and low current density and thickness scalability in a ferroelectric tunnel junction (FTJ). However, the coexistence of ferroelectricity and the semiconducting nature of vdW α-In_2Se_3 have remained a puzzle. As the mobile charges in semiconductors tend to screen the long-range Coulomb interactions and mask any possible FE, most ferroelectrics like barium titanate (BTO) or lead zirconium titanate (PZT) are insulators.

In this work, we successfully realized the growth of a single-crystal monolayer In_2Se_3 with a large grain size up to 200 μm, the largest dimension reported to date. By elaborating the growth conditions, mm-scale size continuous films can be grown with a thickness of around 3 nm. Furthermore, ferroelectric semiconductor junctions (FSJs) are fabricated using both exfoliated films thicker than 70 nm and ultrathin physical vapor deposition (PVD)-grown In_2Se_3 with the thickness scaled down to 3 nm. We propose a model of the depletion-assisted ferroelectric switch for 2D FE semiconductors to explain the presence of ferroelectricity in semiconducting In_2Se_3. Analogous to leaky perovskite crystals, the mobile charge in FE α-In_2Se_3 screens only the bulk part while leaving the surface FE domains in the space charge region undisturbed. As a result, the coercive voltages of the devices are relatively unchanged at 3 and −1 V as the thickness scales range from over 200 to 3 nm.

II. EXPERIMENTS

Many growth models of 2D In_2Se_3 have been proposed to explain the relationship between growth morphology and growth conditions, including source mass, space, substrates, pressure, and flow speed.[20–25] Figure 1(a) illustrates the typical PVD (Physical Vapor Deposition) growth setup used in this work, where In_2Se_3 powder (99.99%, Alfa Aesar) was placed at the hot center of a 1-zone tube furnace with a zone-center temperature of 850 °C. Argon was used as the carrier gas, and In_2Se_3 nanoflakes were deposited on the substrate 13–15 cm away from the heating center. Figure 1(b) shows large-scale In_2Se_3 nanoflakes with different thicknesses grown on mica. Most flakes were aligned in the same direction, indicating vdW epitaxy on mica. Figure S1 in the supplementary material demonstrates the evolution of flake size by increasing the growth time. By carefully tuning the conditions, isolated epitaxial nanoflakes merged into one single domain with lateral

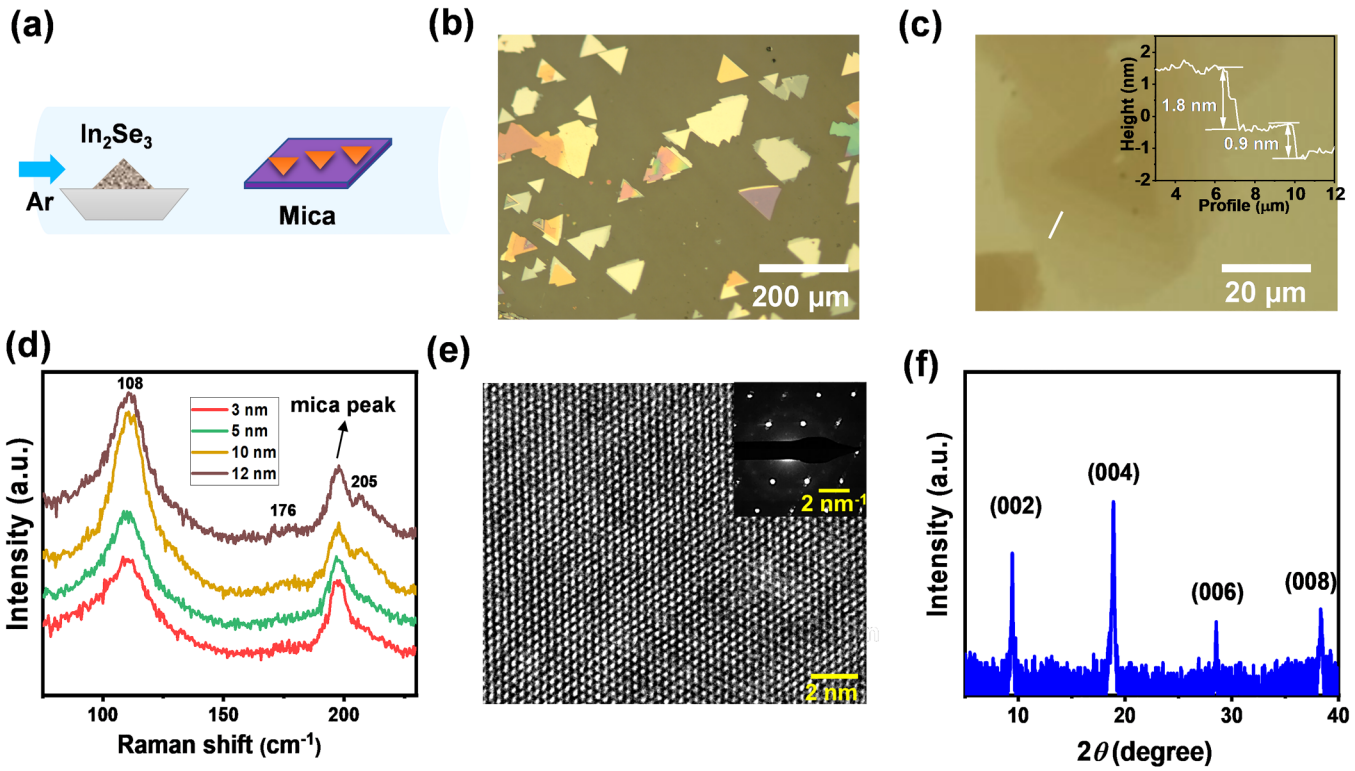

FIG. 1. (a) Schematic of material growth setup using the physical vapor deposition method. (b) Optical image of as-grown In_2Se_3 film with different thicknesses. (c) Optical image of transferred few-layer α-In_2Se_3 nanoflake grown by PVD and then transferred onto Al_2O_3 substrate. Edge height profile was measured by AFM shown in the inset. The white line indicates the approximate location of the AFM profile. (d) Raman spectra of ultrathin In_2Se_3 nanoflakes with different thicknesses grown on mica. (e) HRTEM and SAED patterns of nanoflakes transferred onto a TEM grid. (f) XRD of PVD-grown nanoflakes transferred onto Si.

size up to 200 μm can be achieved, which is, to our knowledge, the largest reported [Fig. S2(a) in the supplementary material]. A wet transfer technique[26] adopted the as-grown flakes from mica onto different substrates (SiO_2, Al_2O_3, etc.) for further characterization and device fabrication. Figure 1(c) shows the optical image of In_2Se_3 nanoflakes transferred onto the Al_2O_3 substrate. Based on the atomic force microscopy (AFM) given in the inset, the smallest step height of ~0.9 nm is consistent with the crystal structure and the layer-by-layer growth mode of In_2Se_3. Similar results of the In_2Se_3 nanoflakes transferred onto a SiO_2 substrate are given in Fig. S2(c) in the supplementary material. Optical images of a-few-layer nanoflakes transferred onto Al_2O_3 are shown in Fig. 1(c) with AFM thickness measurements in the inset. Results for a-few-layer nanoflakes transferred onto a SiO_2 substrate are shown in Fig. S2(c) in the supplementary material. The atomic structures of the nanoflakes were further studied by Raman spectroscopy, XRD, and TEM. Raman spectra of In_2Se_3 nanoflakes with the thickness from 3 to 30 nm are shown in Fig. 1(d). The Raman peaks at 108 cm^{-1}, 180 cm^{-1}, and 205 cm^{-1} are consistent with that from α-In_2Se_3.[22,25] The high-resolution transmission electron microscope (HRTEM) image in Fig. 1(e) and the select area electron diffraction (SAED) patterns given in the inset both confirm the absence of domain boundaries in the PVD-grown $InSe_3$. The XRD of In_2Se_3 nanoflakes wet-transferred onto Si shown in Fig. 1(f) shows only a family of diffraction peaks whose positions indicate a single lattice constant ~19.20, consistent with the (002n) planes of α-In_2Se_3 (PDF No. 34-1279).[23,25] The growth orientation is consistent with the hexagonal structure of In_2Se_3. Although the non-FE β phase sometimes shows up in the vapor-based deposition of In_2Se_3, the various structural characterizations and the FE observed from transport measurements (to be shown later) all show that the nanoflakes synthesized in this work are in the α phase. As for device fabrication, both ~3 nm-thick PVD-grown nanoflakes wet-transferred onto different substrates and >70 nm-thick flakes exfoliated from bulk crystals (purchased from 2Dsemiconductors USA) with a scotch tape were used as channel materials to evaluate the morphology-dependent performance. The same process flow was applied in the subsequent device fabrication for both types of In_2Se_3.

III. RESULTS AND DISCUSSION

Emerging non-volatile memory (e-NVM) technologies such as resistive random-access memory (ReRAM), phase-change memory (PCM), as well as ferroelectric tunnel junctions are regarded as building blocks for next-generation non-von Neumann computing systems. However, such devices suffer from limited dynamic range, high power consumption, and low tunneling current when applied as synaptic devices for crossbar neuromorphic computing systems.[27–29] To overcome these issues, the asymmetric ferroelectric semiconductor junction is proposed to enhance both on-state current and distinction ratio by sandwiching a ferroelectric semiconductor with asymmetric electrodes. Figure 2(a) illustrates the device schematic, where heavily doped p+ Si serves as the bottom gate, 30 nm metal/50 nm Au was deposited as the top electrode, and 15 nm Al_2O_3 was used to isolate the top and bottom electrodes. Figure 2(b) presents an optical image of a fabricated device and a false-color SEM image of the selected region. Ni was first used here as the top electrode for device characterization. Figure 2(c) presents the I–V characteristics of a-FSJ with In_2Se_3 thickness measured as 3 nm by AFM. When the applied voltage is less than the coercive voltage, there is almost no distinction ratio observed. The loop reaches the maximum when the voltage is over the coercive voltage. Eventually shown in Fig. 2(d), the ferroelectric polarization is fully switched. The off-state defined here is based on the relatively lower current density compared to that of the on-state. The main difference between Figs. 2(c) and 2(d) is the maximum voltages applied on the identical 3 nm a-FSJ, 2 and 4 V, respectively. The depletion width is estimated to be ~30 nm from the device simulation indicated in Fig. S3 in the supplementary material, which means that the ultrathin film is already fully depleted in the 3 nm case. As a result, multiple mechanisms including thermal injection and tunneling concurrently govern the transport.[30] Two main factors contribute to a larger current density of both on-state and off-state in Fig. 2(d) than in Fig. 2(c). First, the higher applied voltage generates more mobile carriers with energy larger than the barrier, which causes the current to exponentially increase. Meanwhile, given steep enough band tilting induced by the large polarization charge density when the voltage is larger than the coercive voltage in Fig. 2(d), Fowler–Nordheim tunneling dominates the transport across the triangular potential at the heterojunction in the larger voltage (high-field) regime, which further increases the current density in the ultrathin case. Device performance with a thicker PVD-growth In_2Se_3 nanoflake (20 nm) is also presented in Fig. S3 in the supplementary material. To demonstrate the feasibility of mass production, an mm-scale continuous flake grown by PVD was used to fabricate an array of a-FSJ devices, shown in Fig. S4 (a) in the supplementary material. Strips in light color correspond to the exposed p+ Si bottom electrodes. The transferred, continuous, almost wrinkle-free In_2Se_3 flake appears as a uniform gray area on which metal electrodes were deposited. The thickness of the ultrathin film used here was measured by AFM as 3 nm. The effect of the work functions of contact metals (Ni and Pt) is further investigated to optimize the device performance. The thickness of α-In_2Se_3 films was kept constant for a fair comparison. Sweep voltage was set as 4 V, larger than the coercive voltage of α-In_2Se_3 for full polarization. Figures S4(b)–S4(d) in the supplementary material present the distribution of I–V curves of 5–8 a-FSJ devices on the same thickness film and electrode metals in the metal/α-In_2Se_3/p+ Si structure. It is noticeable that the Ni/α-In_2Se_3/p+ Si structure shows a higher current density of 10–100 A/cm^2 at V = 0.5 V (read voltage) than the device using Pt top contact (0.1–1 A/cm^2). On the other hand, due to the lower work function of Ni (5.1 eV) than Pt (5.6 eV), the on–off ratio of the Ni/α-In_2Se_3/p+ Si structure is ~10^2, one order higher in magnitude than that using Pt top contact. The statistical results of on- and off-current densities and on–off ratio are summarized in Figs. S4(e) and S4(f) in the supplementary material. The large asymmetry in dielectric screening between the metal and p+ Si electrodes plays a significant role in suppressing the off-state current without decreasing the on-state current.

The impact of In_2Se_3 thickness on a-FSJ performance was studied by fabricating devices with PVD-grown In_2Se_3 nanoflakes, whose thickness ranged from 3 to 30 nm and thicker exfoliation

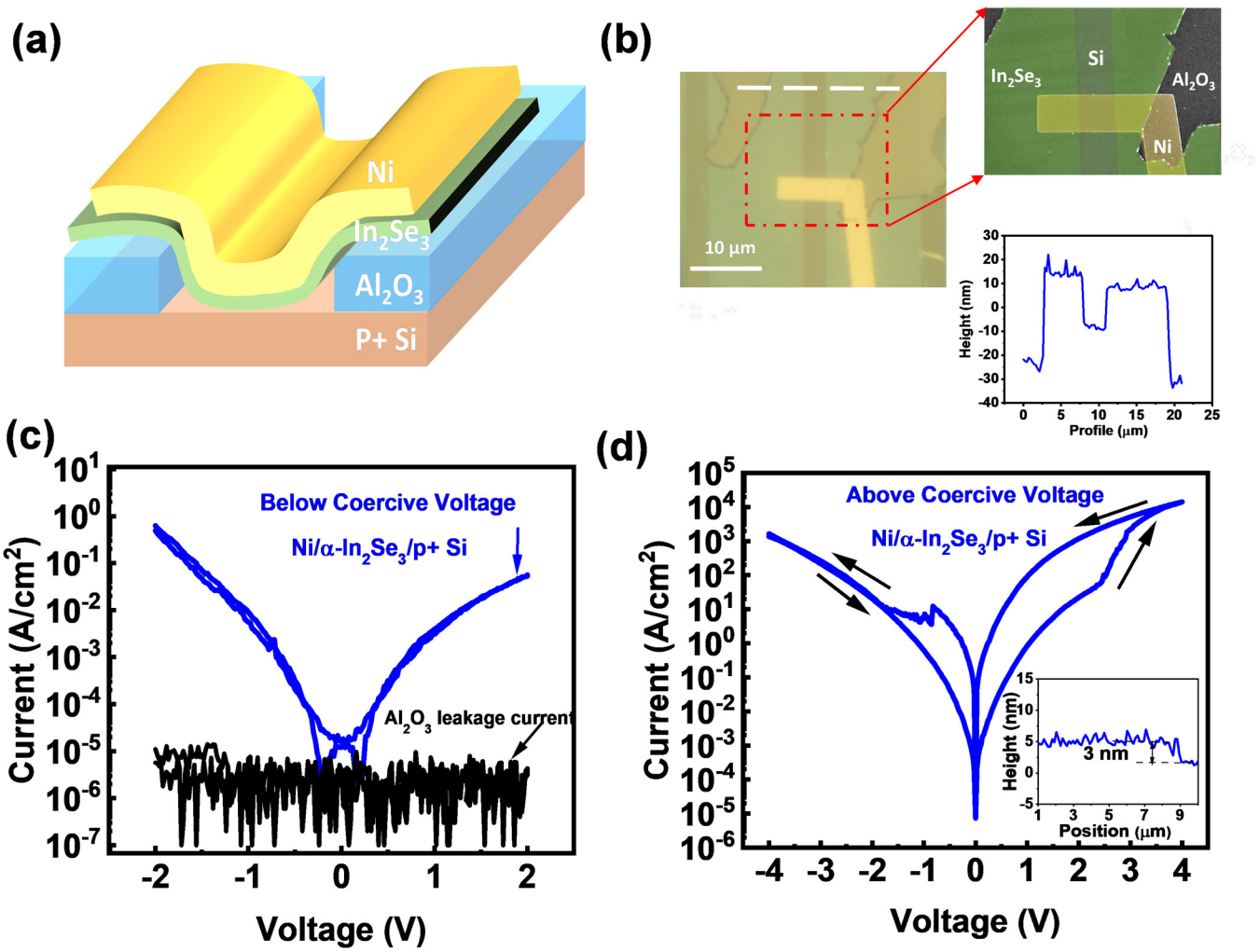

FIG. 2. (a) Schematic of the two-dimensional ferroelectric-semiconductor junction design. (b) Optical image of a-FSJ: transferred In_2Se_3 on 15 nm Al_2O_3/ p+ Si trench structure (left) and the thickness profile measured by AFM. (c) and (d) a-FSJ's I–V characteristics with a voltage sweep below and above the coercive voltage.

In_2Se_3 flakes (thicker than 70 nm), as plotted in Figs. 3(a) and 3(b). It is noted that in the bulk case (thicker than 70 nm), there is no obvious thickness dependence in the current [Fig. 3(b)]. However, in the case of the thin films grown by the PVD method, as the film is fully depleted, tunneling mechanisms (mainly Fowler–Nordheim tunneling) start to dominate the transport, with thermal injection playing a minor role. Given the same voltage applied, a smaller thickness with lower tunneling electroresistance (TER) typically induces a larger current in the ultrathin film. As a result, the current density increases with decreasing In_2Se_3 thickness, as shown in Fig. S5 in the supplementary material. Figure 3(c) further extracts the coercive voltage in forward/reverse scans sustained at approximately 3 and −1 V, respectively, independent of the In_2Se_3 thickness.

To better understand the coexistence of ferroelectricity and transport properties, a COMSOL simulation of the In_2Se_3-Si junction band diagram at equilibrium is carried out as shown in Fig. 4. The simulation structure is composed of Ni/200 nm In_2Se_3/p+ Si 1D a-FSJ for simplification, and the parameters used are listed in Table 1 in the supplementary material. Figures 4(a) and 4(c) show schematics of the polarization states of In_2Se_3. At the left interface, bound charges induced by ferroelectric polarization are screened by the metal electrode, while the right interface between In_2Se_3 and heavily doped Si dominates the ferroelectric behavior, where the depletion and accumulation regions are formed at the on-state and off-state of the device, respectively. Figures 4(b) and 4(d) illustrate the corresponding band diagram calculated where the ferroelectric polarization is induced at the non-linear electric field region at the interface. In equilibrium condition, if In_2Se_3 is thick enough (i.e., thicker than the depletion width), there is negligible voltage drop in the In_2Se_3 layer except for the junction region, including the metal/In_2Se_3 Schottky junction on the left and the In_2Se_3/p+ Si p–n junction on the right. Therefore, the electric field in bulk In_2Se_3

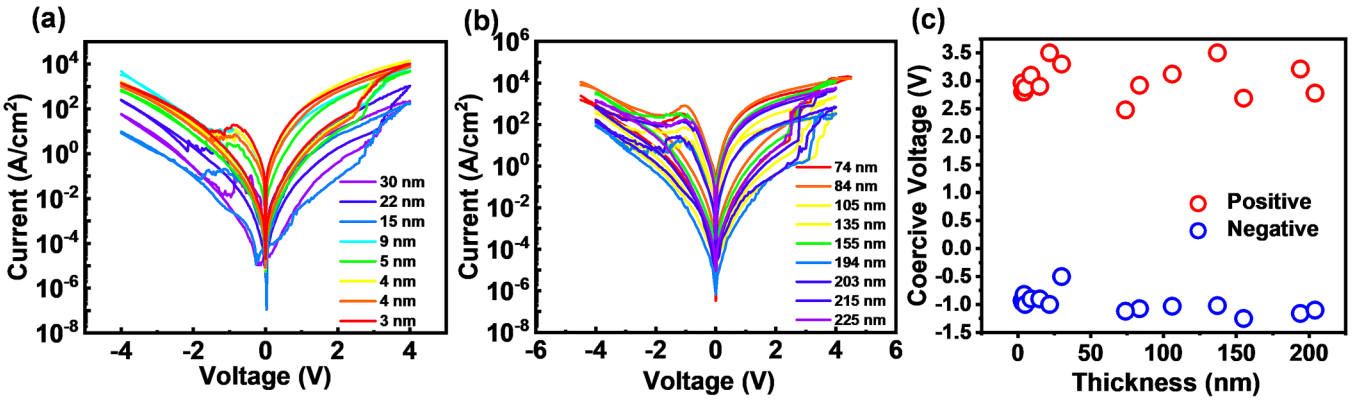

FIG. 3. (a) Thickness-dependent I–V characteristics of PVD-grown α-In_2Se_3 asymmetric c-FSJs. (b) Thickness-dependent I-V characteristics of exfoliated α-In_2Se_3 asymmetric c-FSJs. (c) Thickness-dependent coercive voltage extracted from the I–V characteristics.

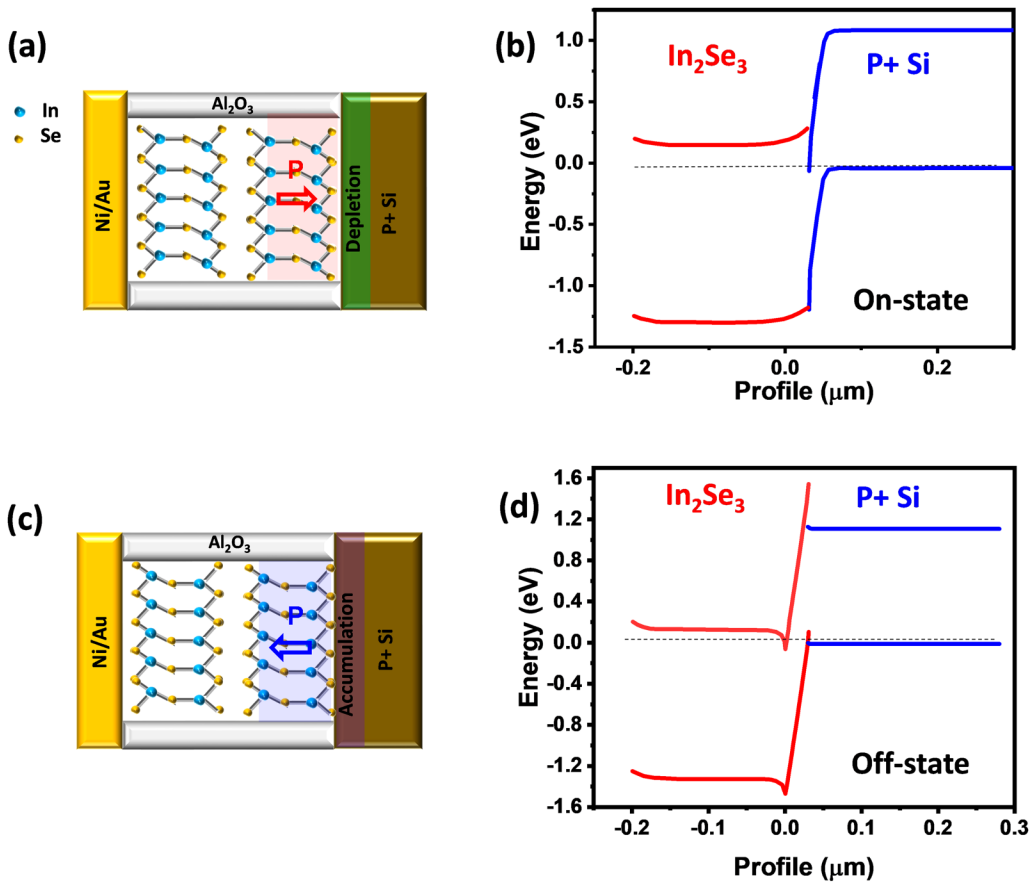

FIG. 4. Quantitative model of ferroelectric switch behavior of a-FSJ and related band-diagram in (a) and (b) on-state and (c) and (d) off-state.

cannot be high enough to trigger ferroelectric polarization. In addition, polarization switching in the Schottky junction is much less compared to the p–n junction because of the existence of band bending in p+ Si, so the properties of a-FSJ in this work can be mainly determined by interface ferroelectric bound charges at the interface between In_2Se_3 and p+ Si. This model qualitatively fits our observations well, which means the nucleation of the ferroelectric domain starts from the surface and remains in the space charge region at the interface within a few layers, while the bulk shows a metallic/semiconducting behavior due to higher electron concentration and mobility. In this way, the coercive voltage is fixed as 3 V in the on-state and −1 V in the off-state due to the asymmetric electric field in different states. The positive coercive voltage and negative coercive voltage are quite different due to the asymmetric junction configuration. This is similar to the conventional p–n junction or the Schottky junction and the electrical properties of these devices are not related to the thickness of semiconductor layers, unless the thickness is less than the thickness of the space charge region. Moreover, a simulation of the ultrathin case was also conducted by COMSOL, and the results are shown in Fig. S4 (a) and S4(b) in the supplementary material. In_2Se_3 is fully depleted in the ultrathin case where the tunneling mechanism cannot be ignored, i.e., Fowler–Nordheim tunneling in the high-field regime. It is observed in our experiment that current density increases with decreasing film thickness below the depletion width like the traditional ferroelectric tunnel junctions. In addition, coercive voltage is the observed constant with thickness scaled-down, which indicates that domain reversal in the ultrathin FE film becomes more difficult due to limited grain size and a higher electric field is needed to finish such a process. Meanwhile, the effect of the ultrathin dead layer at the interface between p+ Si and FE In_2Se_3 becomes more obvious as FE thickness decreases to 3 nm. Therefore, the driving electric field that is really seen by the In_2Se_3 films is decreased, which influences the polarization and contributes to a higher coercive field in the wholescale.[31] Further investigation is needed to elaborate on the details of the domain wall properties and complex multiple transport mechanisms, especially, the thickness, voltage, and temperature dependency in a-FSJ.

IV. SUMMARY AND CONCLUSIONS

In summary, we have demonstrated a-FSJ based on PVD-growth In_2Se_3 with the thickness scaled down to ∼3 nm. Both large read current density of ∼100 A/cm^2 and distinction ratio of over 10^2 are achieved on mm-scale continuous film at a low read voltage. In addition, a model of the polarization switching process in ferroelectric semiconductor junction is developed to explain its unique thickness scaling behaviors. Coercive voltages of ferroelectric semiconductor junctions based on In_2Se_3 are nearly constant at 3 and −1 V as In_2Se_3 thicknesses reduce from 200 to 3 nm. It is inferred from the thickness-independent coercive voltage that the ferroelectric polarization arises from the surface and remains undisturbed in the depletion region, while inside the bulk of In_2Se_3, ferroelectric domains are randomly aligned, canceling out any net polarization by free charges. The experimental results are consistent with the proposed polarization mechanism in ferroelectric semiconductor junctions. Our results shed light on the origin of ferroelectric switching behavior in two-dimensional ferroelectric semiconductor junctions and pave the way for next-generation ultrathin ferroelectric semiconductor memories.

SUPPLEMENTARY MATERIAL

See the supplementary material for time-dependent material growth evolvement, optical images of large-domain single-crystal In_2Se_3 and flakes transferred onto different substrates, the performance of 20 nm PVD-growth In_2Se_3 a-FSJ, a-FSJ array based on mm-scale In_2Se_3 film grown by PVD and related contact study of Pt and Ni, the thickness-dependent current density of PVD-growth In_2Se_3 a-FSJ, and simulation results of 1D a-FSJ.

ACKNOWLEDGMENTS

The authors would like to thank Kumar Virwani, Brian Doyle, and Derchang Kau for the valuable discussions. This work is supported by Intel Corporation.

AUTHOR DECLARATIONS

Conflict of Interest

The authors have no conflicts to disclose.

Author Contributions

Dongqi Zheng: Data curation (equal); Formal analysis (equal); Investigation (equal). **Mengwei Si:** Data curation (equal); Formal analysis (equal); Investigation (equal). **Sou-Chi Chang:** Investigation (equal); Methodology (equal). **Nazila Haratipour:** Investigation (equal); Supervision (equal). **Zhizhong Chen:** Data curation (equal). **Adam Charnas:** Data curation (equal). **Shouyuan Huang:** Data curation (equal). **Kang Wang:** Data curation (equal). **Letian Dou:** Supervision (equal). **Xianfan Xu:** Supervision (equal). **Uygar E. Avci:** Supervision (equal). **Peide D. Ye:** Conceptualization (equal); Supervision (equal).

DATA AVAILABILITY

The data that support the findings of this study are available from the corresponding author upon reasonable request.

REFERENCES

[1]L. Qi, S. Ruan, and Y.-J. Zeng, Adv. Mater. **33**, 2005098 (2021).
[2]M. Wu, ACS Nano **15**, 9229 (2021).
[3]E. Y. Tsymbal, Science **372**, 1389 (2021).
[4]F. Liu, L. You, K. L. Seyler, X. Li, P. Yu, J. Lin, X. Wang, J. Zhou, H. Wang, H. He, S. T. Pantelides, W. Zhou, P. Sharma, X. Xu, P. M. Ajayan, J. Wang, and Z. Liu, Nat. Commun. **7**, 12357 (2016).
[5]K. Chang, J. Liu, H. Lin, N. Wang, K. Zhao, A. Zhang, F. Jin, Y. Zhong, X. Hu, W. Duan, Q. Zhang, L. Fu, Q.-K. Xue, X. Chen, and S.-H. Ji, Science **353**, 274 (2016).
[6]K. Chang, F. Küster, B. J. Miller, J. R. Ji, J. L. Zhang, P. Sessi, S. Barraza-Lopez, and S. S. P. Parkin, Nano Lett. **20**, 6590 (2020).
[7]C. Zheng, L. Yu, L. Zhu, J. L. Collins, D. Kim, Y. Lou, C. Xu, M. Li, Z. Wei, Y. Zhang, M. T. Edmonds, S. Li, J. Seidel, Y. Zhu, J. Z. Liu, W.-X. Tang, and M. S. Fuhrer, Sci. Adv. **4**(7), eaar7720 (2018).
[8]W. Ding, J. Zhu, Z. Wang, Y. Gao, D. Xiao, Y. Gu, Z. Zhang, and W. Zhu, Nat. Commun. **8**, 1 (2017).

[9]Z. Chen, Y. Hu, L. Zhang, J. Jiang, R. Hawks, and J. Shi, Appl. Phys. Lett. **119**, 033103 (2021).
[10]J. Ding, D. F. Shao, M. Li, L. W. Wen, and E. Y. Tsymbal, Phys. Rev. Lett. **126**, 057601 (2021).
[11]X. Tao and Y. Gu, Nano Lett. **13**(8), 3501–3505 (2013).
[12]M. Dai, K. Li, F. Wang, Y. Hu, J. Zhang, T. Zhai, B. Yang, Y. Fu, W. Cao, D. Jia, Y. Zhou, and P. A. Hu, Adv. Elect. Mater. **6**, 1900975 (2020).
[13]C. Gong, E. M. Kim, Y. Wang, G. Lee, and X. Zhang, Nat. Commun. **10**, 2657 (2019).
[14]A. K. Saha, M. Si, P. D. Ye, and S. K. Gupta, Appl. Phys. Lett. **117**, 183504 (2020).
[15]F. Xue, X. He, J. R. D. Retamal, A. Han, J. Zhang, Z. Liu, J. K. Huang, W. Hu, V. Tung, J. H. He, L. J. Li, and X. Zhang, Adv. Mater. **31**, 1901300 (2019).
[16]J. Xiao, H. Zhu, Y. Wang, W. Feng, Y. Hu, A. Dasgupta, Y. Han, Y. Wang, D. A. Muller, L. W. Martin, P. Hu, and X. Zhang, Phys. Rev. Lett. **120**, 227601 (2018).
[17]F. Xue, W. Hu, K.-C. Lee, L.-S. Lu, J. Zhang, H.-L. Tang, A. Han, W.-T. Hsu, S. Tu, W.-H. Chang, C.-H. Lien, J.-H. He, Z. Zhang, L.-J. Li, and X. Zhang, Adv. Funct. Mater. **28**, 1803738 (2018).
[18]M. Si, A. K. Saha, S. Gao, G. Qiu, J. Qin, Y. Duan, J. Jian, C. Niu, H. Wang, W. Wu, S. K. Gupta, and P. D. Ye, Nat. Elect. **2**, 580 (2019).
[19]M. Si, Z. Zhang, S. C. Chang, N. Haratipour, D. Zheng, J. Li, U. E. Avci, and P. D. Ye, ACS Nano **15**, 5689 (2021).
[20]L. Tang, C. Teng, Y. Luo, U. Khan, H. Pan, Z. Cai, Y. Zhao, B. Liu, and H.-M. Cheng, Research **2019**, 2763704 (2019).
[21]J. Zhou, Q. Zeng, D. Lv, L. Sun, L. Niu, W. Fu, F. Liu, Z. Shen, C. Jin, and Z. Liu, Nano Lett. **15**, 6400 (2015).
[22]S. M. Poh, S. J. R. Tan, H. Wang, P. Song, I. H. Abidi, X. Zhao, J. Dan, J. Chen, Z. Luo, S. J. Pennycook, A. H. Castro Neto, and K. P. Loh, Nano Lett. **18**, 6340 (2018).
[23]M. Küpers, P. M. Konze, A. Meledin, J. Mayer, U. Englert, M. Wuttig, and R. Dronskowski, Inorg. Chem. **57**, 11775 (2018).
[24]R. Rashid, F. C. C. Ling, S. P. Wang, K. Xiao, X. Cui, T. H. Chan, H. C. Ong, W. Azeem, and M. Younas, Nanoscale **12**, 20189 (2020).
[25]Y. Hu, W. Feng, M. Dai, H. Yang, X. Chen, G. Liu, S. Zhang, and P. Hu, Semicond. Sci. Technol. **33**, 125002 (2018).
[26]A. Gurarslan, Y. Yu, L. Su, Y. Yu, F. Suarez, S. Yao, Y. Zhu, M. Ozturk, Y. Zhang, and L. Cao, ACS Nano **8**, 11522 (2014).
[27]J. J. Yang, D. B. Strukov, and D. R. Stewart, Nat. Nanotechnol. **8**, 13 (2013).
[28]H. S. P. Wong, S. Raoux, S. Kim, J. Liang, J. P. Reifenberg, B. Rajendran, M. Asheghi, and K. E. Goodson, Proc. IEEE. **98**, 2201 (2010).
[29]A. Chanthbouala, A. Crassous, V. Garcia, K. Bouzehouane, S. Fusil, X. Moya, J. Allibe, B. Dlubak, J. Grollier, S. Xavier, C. Deranlot, A. Moshar, R. Proksch, N. D. Mathur, M. Bibes, and A. Barthélémy, Nat. Nanotech. **7**, 101 (2012).
[30]D. Pantel and M. Alexe, Phys. Rev. B **82**, 134105 (2010).
[31]J. Pérez de la Cruz, E. Joanni, P. M. Vilarinho, and A. L. Kholkin, J. Appl. Phys. **108**, 114106 (2010).